Draft version September 22, 2020
Typeset using LaTeX **modern** style in AASTeX63

Detection of CH_3C_3N in Titan's Atmosphere

Alexander E. Thelen,[1,2] Martin A. Cordiner,[1,3] Conor A. Nixon,[1]
Véronique Vuitton,[4] Zbigniew Kisiel,[5] Steven B. Charnley,[1]
Maureen Y. Palmer,[6] Nicholas A. Teanby,[7] and Patrick G. J. Irwin[8]

[1]*Solar System Exploration Division, NASA Goddard Space Flight Center, Greenbelt, MD 20771, USA*
[2]*Universities Space Research Association, Columbia, MD 21046, USA†*
[3]*Department of Physics, Catholic University of America, Washington, DC 20064, USA*
[4]*Institut de Planétologie et d'Astrophysique de Grenoble, Université Grenoble Alpes, CNRS, Grenoble 38000, France*
[5]*Institute of Physics, Polish Academy of Sciences, Al. Lotników 32/46, 02-668 Warszawa, Poland*
[6]*Lunar and Planetary Laboratory, University of Arizona, Tucson, AZ 85721, USA*
[7]*School of Earth Sciences, University of Bristol, Bristol BS8 1RJ, UK*
[8]*Atmospheric, Oceanic and Planetary Physics, Clarendon Laboratory, University of Oxford, Oxford, OX1 3PU, UK*

ABSTRACT

Titan harbors a dense, organic-rich atmosphere primarily composed of N_2 and CH_4, with lesser amounts of hydrocarbons and nitrogen-bearing species. As a result of high sensitivity observations by the Atacama Large Millimeter/submillimeter Array (ALMA) in Band 6 (∼230–272 GHz), we obtained the first spectroscopic detection of CH_3C_3N (methylcyanoacetylene or cyanopropyne) in Titan's atmosphere through the observation of seven transitions in the $J = 64 \rightarrow 63$ and $J = 62 \rightarrow 61$ rotational bands. The presence of CH_3C_3N on Titan was suggested by the Cassini Ion and Neutral Mass Spectrometer detection of its protonated form: $C_4H_3NH^+$, but the atmospheric abundance of the associated (deprotonated) neutral product is not well constrained due to the lack of appropriate laboratory reaction data. Here, we derive the column density of CH_3C_3N to be $(3.8–5.7)\times10^{12}$ cm^{-2} based on radiative transfer models sensitive to altitudes above 400 km Titan's middle atmosphere. When compared with laboratory and photochemical model results, the detection of methylcyanoacetylene provides important constraints for the determination of the associated production pathways (such as those involving CN, CCN, and hydrocarbons), and reaction rate coefficients. These results also further demonstrate the importance of ALMA and (sub)millimeter spectroscopy for future investigations of Titan's organic inventory and atmospheric chemistry, as CH_3C_3N marks the heaviest polar molecule detected spectroscopically in Titan's atmosphere to date.

Corresponding author: Alexander E. Thelen
alexander.e.thelen@nasa.gov

† NASA Astrobiology Postdoctoral Program Fellow

1. INTRODUCTION

The atmosphere of Titan, the largest moon of Saturn, is primarily composed of N_2 (∼95–98%) and CH_4 (∼1–5%). A plethora of trace organic compounds makes up the remaining atmospheric composition, which are formed through the photodissociation of nitrogen and methane, and interactions with the Saturnian magnetosphere or galactic cosmic rays (GCR) (Loison et al., 2015; Vuitton et al., 2019). The formation of complex atmospheric species – such as nitriles ($C_XH_Y[CN]_Z$) – in Titan's upper atmosphere, their condensation and accumulation in the stratospheric haze layer, and participation in the methane-based meteorological cycle, are important processes that influence not only Titan's global climate but also the connection between the atmosphere and the organic regolith and hydrocarbon lakes. In addition to increasing our understanding of Titan's atmospheric and surface properties, knowledge of Titan's atmospheric photochemistry and the extent of its molecular inventory are important for assessing Titan's potential for habitability (Hörst et al., 2012; Palmer et al., 2017).

While numerous heavy ion species were detected with the Ion and Neutral Mass Spectrometer (INMS) and Cassini Plasma Spectrometer instruments onboard the Cassini spacecraft at altitudes ∼1000–1200 km, these measurements did not fully resolve the identities of many large species – particularly those with a mass-to-charge ratio (m/z) > 60. Among these, the detection of ions with $m/z = 66$, attributed to $C_4H_3NH^+$ (Vuitton et al., 2007), presented the case for multiple associated neutral species: CH_3C_3N (methylcyanoacetylene or cyanopropyne, hereafter the former) or $H_2CCCHCN$ (cyanoallene). Laboratory experiments predict the formation of both C_4H_3N isomers in Titan's atmosphere through crossed molecular beam (Huang et al., 1999; Balucani et al., 2000) and plasma discharge (Thompson et al., 1991; Coll et al., 1999; Molina-Cuberos et al., 2002) experiments under Titan-like (N_2/CH_4-rich) conditions. However, while both methylcyanoacetylene and cyanoallene have been detected previously in the interstellar medium toward the Sgr B2 high-mass star-forming region and in the nearby molecular cloud TMC-1 (Broten et al., 1984; Lovas et al., 2006; Belloche et al., 2013), the C_4H_3N isomers have yet to be detected in the atmosphere of Titan.

The advent of the Atacama Large Millimeter/submillimeter Array (ALMA) in the past decade has enabled the exploration of Titan's atmospheric composition and dynamics to an unprecedented degree from the ground, allowing for follow-up studies on the distribution of trace molecular species by the *Voyager-1* and Cassini-Huygens missions. Comprised of many 12 m antennas spatially separated by up to 16 km and access to frequencies ranging from ∼84–950 GHz (∼3.5–0.3 mm), ALMA has enabled the detection of new molecular species (Cordiner et al., 2015; Palmer et al., 2017; Nixon et al., 2020), isotopes (Serigano et al., 2016; Molter et al., 2016; Thelen et al., 2019a; Iino et al., 2020), and vibrationally excited transitions (Cordiner et al., 2018; Kisiel et al., 2020) in Titan's atmosphere. The spectral and spatial resolution capabilities of ALMA have also provided the means by which to map the distribution

and dynamics of many nitrogen-bearing molecules (Cordiner et al., 2014; Lai et al., 2017; Thelen et al., 2019b; Cordiner et al., 2019; Lellouch et al., 2019), allowing for the study of atmospheric variations throughout Titan's long (29.5 yr) seasonal cycle after the end of the Cassini mission in 2017.

Here, we detail the first results of deep ALMA Cycle 8 observations of Titan during November and December, 2019. The high sensitivity of these data have allowed for the spectroscopic detection of two CH_3C_3N bands for the first time in Titan's atmosphere (or indeed the atmosphere of any Solar System body).

2. OBSERVATIONS

Titan was observed across multiple execution blocks between November 14 and December 16, 2019, under ALMA Project Code #2019.1.00783.S. Integrations on Titan were distributed across three Science Goals (SG). SG1, which targeted the CO $J = 2 \rightarrow 1$ transition at 230.538 GHz to retrieve Titan's disk-averaged temperature profile, was observed on November 14, 2019 for 11.59 min with 44 antennas. SG2 and SG3 covered multiple nitrile species, their C- and N-isotopes (e.g. $H^{13}CCCN$, $HCCC^{15}N$), and potential isocyanide species. Observations for these two Science Goals required seven executions between November 25 to December 16, 2019, with 43–45 antennas; the cumulative integration time on Titan was 81.65 min for SG3 and 175.4 min for SG2, which required the highest spectral sensitivity ($\sim$1 mJy). Spectra from all three Science Goals were analyzed for the detection and subsequent radiative transfer modeling of CO and CH_3C_3N transitions.

ALMA visibility data were calibrated with version 5.6.1-8 of the Common Astronomy Software Applications (CASA) pipeline using the scripts provided by the Joint ALMA Observatory (JAO). In addition to Titan, the quasars J1924-2914, J1911-2006, and J2056-4714 were also observed for the purposes of flux, bandpass, and phase calibrations. Subsequent executions of the pipeline calibrations were completed after modifying the JAO scripts to implement a variety of bandpass smoothing intervals to improve the spectral root mean square (RMS) noise (particularly in SG2, with the longest total integration time) without significantly degrading the bandpass shape. See Appendix A for the results and discussion of the effects of bandpass smoothing on these ALMA observations.

The CASA `tclean` procedure was performed on the resulting calibrated visibility measurement sets to deconvolve the complex interferometric point-spread function (PSF) and reconstruct the brightness distribution of Titan in standard spatial coordinates. The `Högbom` algorithm was used during deconvolution with "natural" weighting applied to prioritize the image signal-to-noise ratio (SNR). The `tclean` image sizes and pixel scales were set to 270×270 $0.16''$-pixels for SG1, 224×224 $0.17''$-pixels for SG2, and 210×210 $0.18''$-pixels for SG3, so as to sufficiently sample the ALMA PSF ($\sim$5 pixels across the full width at half maximum). Images produced through concatenated integrations (SG2, SG3) were set to use a common synthesized

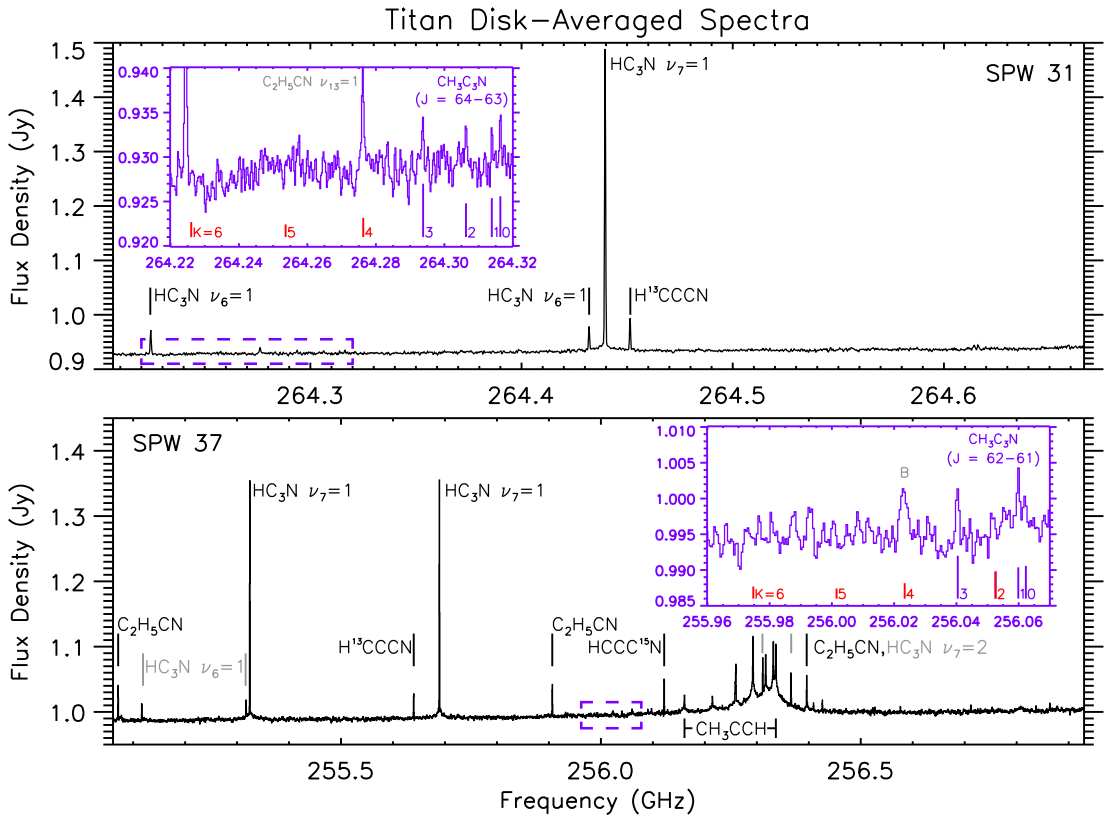

Figure 1. Disk-averaged spectra of Titan from SG2 and SG3 spectral windows 31 (top) and 37 (bottom), respectively. Strong spectral lines of various molecular species are marked with black or gray lines; spectral line parameters are detailed in Table 1. Additional unlabeled transitions of C_2H_5CN and C_2H_3CN are present. Insets in purple show the detections of the CH_3C_3N $K = 0$–3 lines in the $J = 64 \rightarrow 63$ and $J = 62 \rightarrow 61$ bands. Both detected transitions (purple) and undetected or blended transitions (red) are marked, with marker heights proportional to the line intensities (calculated at 160 K). An additional, blended feature (B) is shown in the inset of SPW 37 at $\sim$ 256.024 GHz, most likely a combination of C_3H_8, C_2H_5CN, and CH_3C_3N.

beam shape (the ALMA PSF), and were corrected for the ALMA primary beam. The resulting images had beam sizes equal to $1.276'' \times 0.933''$ for SG1, $1.470'' \times 1.067''$ for SG2, and $1.553'' \times 1.142''$ for SG3. As Titan's angular diameter (with its extended atmosphere up to 1200 km) was between 0.954″–0.985″ during these observations, we were unable to investigate potential spatial variation in the atmospheric distribution of CH_3C_3N from these images. The resulting disk-averaged spectra of spectral windows (SPW) 31 (SG2) and 37 (SG3) are shown in Figure 1, including the detections of the CH_3C_3N $J = 64 \rightarrow 63$ and $J = 62 \rightarrow 61$ bands, respectively, in the panel insets. The inherent channel spacing of the SG2 and SG3 spectral windows were 244 and 488 kHz, respectively, resulting in spectral resolutions of 488 and 976 kHz after Hanning smoothing by the correlator. A number of additional transitions from other molecular species were detected in these two spectral windows, which are detailed in Table 1. While the CH_3C_3N $J = 62 \rightarrow 61$, $K = 2$ transition at 256.053 GHz was

not detected above the noise in SG3 SPW 37, seven other CH_3C_3N transitions were detected between both spectral windows.

3. RADIATIVE TRANSFER MODELING & RESULTS

Disk-averaged data were extracted from spectral image cubes using a circular mask that encompassed pixels with $\geq$ 90% of Titan's continuum flux (Lai et al., 2017; Thelen et al., 2019a; Nixon et al., 2020). Variations in Titan's distance and relative velocity between integrations were accounted for in the previous calibration and imaging steps. We used 36 line-of-sight emission angles to properly characterize Titan's disk-averaged radiance from the surface to 1200 km (Teanby et al., 2013; Thelen et al., 2018, 2019b), and applied small multiplicative factors to the spectra to resolve differences between the data and synthetic spectra in continuum regions (scaling factors on the order 1.15; see Thelen et al., 2018). We employed the Non-linear optimal Estimator for Multi-variatE spectral analySIS (NEMESIS) radiative transfer package (Irwin et al., 2008) to model Titan's atmospheric emission and retrieve vertical temperature and abundance profiles, as has been used previously for Cassini Composite Infrared Spectrometer and ALMA observations of Titan (see, for example, Nixon et al., 2010, Teanby et al., 2010). The NEMESIS atmospheric model parameterization we used follows the prescription of previous studies of Titan with ALMA (Thelen et al., 2018, 2019a,b). Spectral line parameters from the Cologne Database for Molecular Spectroscopy (CDMS; Müller et al., 2001; Müller et al., 2005; Endres et al., 2016) were used for models of CH_3C_3N (Moïses et al., 1982; Bester et al., 1984, 1985; with purely K-dependent line parameters taken from CH_3CN, Anttila et al., 1993). The excited state C_2H_5CN lines not yet available in CDMS (e.g. Fig. 1, top inset) were taken from Kisiel et al. (2020).

We first retrieved Titan's disk-averaged temperature profile by modeling the CO $J = 2 \rightarrow 1$ transition from SG1 SPW 29 (Fig. 2, top panel) by holding the CO vertical abundance profile constant at 49.6 ppm due to the molecule's long photochemical lifetime in Titan's atmosphere (Serigano et al., 2016; Thelen et al., 2018). The *a priori* temperature profile was produced through a combination of the retrieved disk-averaged profile from ALMA observations of Titan in 2015 (Thelen et al., 2018) from lower stratospheric altitudes through the mesosphere ($\sim$100–600 km), and from the Cassini radio-science and Huygens Atmospheric Structure Instrument temperature measurements in the troposphere (Fulchignoni et al., 2005; Schinder et al., 2012). The temperature profile was allowed to vary continuously throughout the atmosphere, with *a priori* uncertainties initially set to 5 K and a correlation length of 1.5 scale heights to sufficiently reduce artificial vertical oscillations in the retrieved profile. The resulting temperature profile is shown in Fig. 2 (bottom panel), which was then used to model the CH_3C_3N spectral bands from SG2 and SG3. As noted in previous ALMA studies, the (sub)mm lines of CO in Titan's atmosphere allow for the measurement of temperature throughout the stratosphere and into the lower mesosphere, which

Table 1. Spectral Transitions

Species	Rest Freq. (GHz)	Transition[a]	E'' (K)	SG	Spw
CO	230.538	$2 \rightarrow 1$	17	1	29
HC_3N	255.116	$28 \rightarrow 27$, $\nu_6 = 1f$	895	3	37
HC_3N	255.317	$28 \rightarrow 27$, $\nu_6 = 1e$	895	3	37
HC_3N	264.224	$29 \rightarrow 28$, $\nu_6 = 1e$	908	2	31
HC_3N	264.431	$29 \rightarrow 28$, $\nu_6 = 1f$	908	2	31
HC_3N	255.324	$28 \rightarrow 27$, $\nu_7 = 1f$	499	3	37
HC_3N	255.689	$28 \rightarrow 27$, $\nu_7 = 1e$	499	3	37
HC_3N	264.439	$29 \rightarrow 28$, $\nu_7 = 1e$	511	2	31
HC_3N	256.311	$28 \rightarrow 27$, $\nu_7 = 2f$	823	3	37
HC_3N	256.365	$28 \rightarrow 27$, $\nu_7 = 2e$	823	3	37
$H^{13}CCCN$	255.639	$29 \rightarrow 28$	184	3	37
$H^{13}CCCN$	264.451	$30 \rightarrow 29$	197	2	31
$HCCC^{15}N$	256.121	$29 \rightarrow 28$	184	3	37
C_2H_5CN	255.071	$28_{2,26} \rightarrow 27_{2,25}$	182	3	37
C_2H_5CN	255.906	$28_{3,25} \rightarrow 27_{3,24}$	186	3	37
C_2H_5CN	256.396	$29_{1,28} \rightarrow 28_{1,27}$	189	3	37
C_2H_5CN	264.276	$29_{4,26} \rightarrow 28_{4,25}$, $\nu_{13} = 1$	502	2	31
CH_3CCH	256.097	$15_7 \rightarrow 14_7$	452	3	37
CH_3CCH	256.161	$15_6 \rightarrow 14_6$	358	3	37
CH_3CCH	256.214	$15_5 \rightarrow 14_5$	279	3	37
CH_3CCH	256.258	$15_4 \rightarrow 14_4$	214	3	37
CH_3CCH	256.293	$15_3 \rightarrow 14_3$	163	3	37
CH_3CCH	256.317	$15_2 \rightarrow 14_2$	127	3	37
CH_3CCH	256.332	$15_1 \rightarrow 14_1$	106	3	37
CH_3CCH	256.337	$15_0 \rightarrow 14_0$	98	3	37
CH_3C_3N	255.975	$62_6 \rightarrow 61_6$	656	3	37
CH_3C_3N	256.001	$62_5 \rightarrow 61_5$	574	3	37
CH_3C_3N	256.023	$62_4 \rightarrow 61_4$	507	3	37
CH_3C_3N	256.040	$62_3 \rightarrow 61_3$	455	3	37
CH_3C_3N	256.053	$62_2 \rightarrow 61_2$	417	3	37
CH_3C_3N	256.060	$62_1 \rightarrow 61_1$	395	3	37
CH_3C_3N	256.062	$62_0 \rightarrow 61_0$	387	3	37
CH_3C_3N	264.226	$64_6 \rightarrow 63_6$	682	2	31
CH_3C_3N	264.254	$64_5 \rightarrow 63_5$	599	2	31
CH_3C_3N	264.276	$64_4 \rightarrow 63_4$	532	2	31
CH_3C_3N	264.294	$64_3 \rightarrow 63_3$	480	2	31
CH_3C_3N	264.306	$64_2 \rightarrow 63_2$	442	2	31
CH_3C_3N	264.314	$64_1 \rightarrow 63_1$	420	2	31
CH_3C_3N	264.316	$64_0 \rightarrow 63_0$	412	2	31

NOTE—Rows in red denote undetected (often higher energy) CH_3C_3N transitions. [a]Rotational transitions are written as $J'' \rightarrow J'$, $J''_{K''} \rightarrow J'_{K'}$, or $J''_{K''_a,K''_c} \rightarrow J'_{K'_a,K'_c}$.

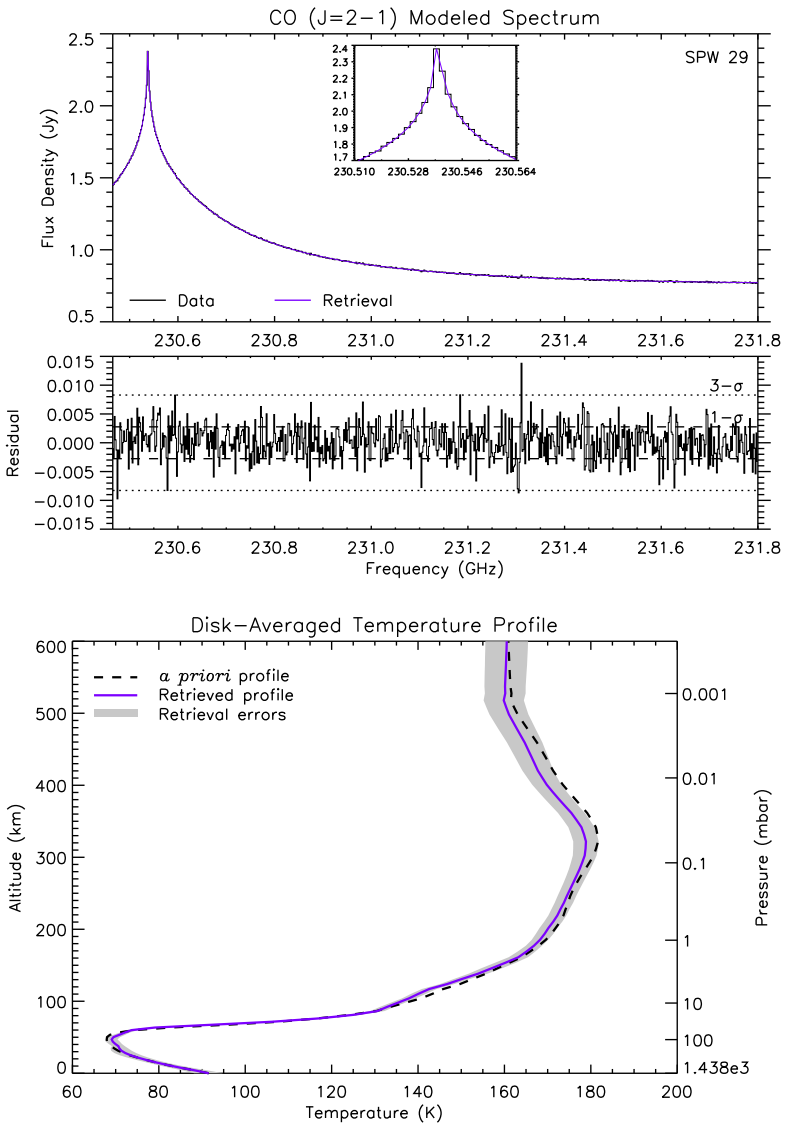

Figure 2. (Top) ALMA disk-averaged spectrum (black) of the CO $J = 2 \rightarrow 1$ transition, with the best-fit NEMESIS model after retrieving Titan's vertical temperature profile (purple). The residual (data minus model) spectrum is shown below with 1-σ (dashed) and 3-σ (dotted) RMS values. (Bottom) The corresponding retrieved temperature profile (purple) and error envelope (gray). The *a priori* temperature profile is shown (dashed black) from previous ALMA and Cassini observations.

is most notable in Fig. 2 (bottom panel) where the retrieved temperature profile departs from the *a priori* temperature profile at altitudes ∼100–530 km (∼10–10^{-3} mbar). Above 600 km, temperatures were set as an isothermal profile at 160 K.

As transitions from numerous other trace species are found in both SG2 and SG3 spectral windows containing CH_3C_3N (Fig. 1), we included the disk-averaged abundance profiles of C_3H_4, HC_3N (and its isotopes), and C_2H_5CN from previous ALMA studies of Titan's atmosphere (Thelen et al., 2019b; Cordiner et al., 2015; Lai et al., 2017) in models of CH_3C_3N bands to correctly fit the continuum and contributions

from nearby line wings. To mitigate the influence of these interloping species and best constrain the retrieved CH_3C_3N abundance profiles, we only modeled spectral regions covering the $K = 0$–3 transitions, as higher energy lines were not detected in either CH_3C_3N band. Due to the unknown nature (both in shape and relative abundance) of the vertical CH_3C_3N mixing ratio profile, we attempted to fit both detected spectral bands with a variety of vertical profiles. Previous ALMA studies found that relatively narrow spectral lines (such as C_2H_3CN, C_2H_5CN, c-C_3H_2) that sound Titan's upper stratosphere and mesosphere could be adequately fit using vertical profiles consisting of constant mixing ratios above a certain altitude (step profiles), or profiles that are linear in log-pressure space (Cordiner et al., 2015; Palmer et al., 2017; Teanby et al., 2018; Nixon et al., 2020). Additionally, photochemical models of Titan's atmosphere (Loison et al., 2015; Vuitton et al., 2019) make predictions for the vertical profile of CH_3C_3N and other trace species, which can then be tested through radiative transfer modeling. As the spectral resolution in these ALMA observations are relatively high and include few spectral lines, we ran NEMESIS in the more accurate line-by-line mode as opposed to utilizing the correlated-k method as is done for infrared and visible wavelengths. We fit both spectral windows separately for independent confirmation of the retrieved CH_3C_3N abundance profiles, and in all cases found the resulting abundances between the two spectral windows to agree within the 1-σ retrieval errors. We report the final abundances as a weighted mean of each pair of retrievals; the RMS of our SG2 data is $\sim \sqrt{2}$ less than that of SG3 (see Appendix A). A variety of synthetic model spectra corresponding to the vertical profile retrievals detailed below are shown for both bands of CH_3C_3N in Fig. 3A and B, with the weighted mean best fit profiles shown in Fig. 3C compared to the photochemical model of Loison et al. (2015). The retrieved abundances and calculated column densities for these profiles are detailed in Table 2.

First, we attempted to fit both CH_3C_3N spectral bands with a range of step profiles from 100–800 km with uniform abundance at every 100 km interval, initially set at a test value of 2.5 ppb. Profiles were then scaled iteratively by NEMESIS until converging upon a fit that sufficiently minimized the reduced-χ^2 value, which was found to be similar for all step profiles above 400 km (Table 2). Below these altitudes, the synthetic CH_3C_3N line wings contribute too much to obtain a good fit (i.e. $\chi^2/n >$ 1); an example is shown in Fig. 3A and B for a 300 km step model (red spectrum). Between 400–800 km, the spectral fits do not differ significantly (Table 2). Here, we find the total integrated column density of CH_3C_3N to range between (3.86–5.73)$\times 10^{12}$ from the best fit step models (Fig. 3C, orange dashed lines).

Next, a linear gradient was parameterized by allowing NEMESIS to vary the abundance and pressure between two points, with zero abundance below the high-pressure point (Point 1, with pressure p_1 and abundance q_1) and constant abundance above the low-pressure point (Point 2, with pressure p_2 and abundance q_2). While the p_1 and q_1 values were initially set with fairly arbitrary values with large errors to allow

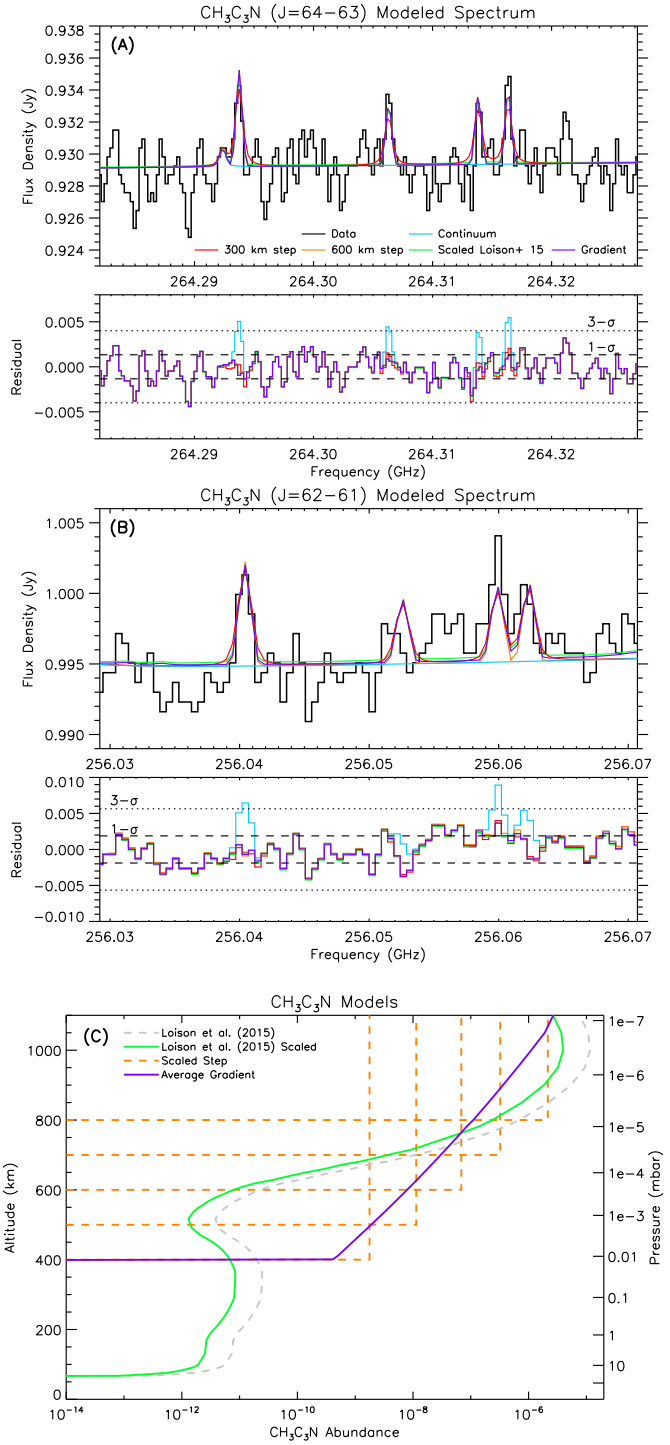

Figure 3. (A) Disk-averaged spectrum of CH_3C_3N $J = 64 \rightarrow 63$ (black) compared to various NEMESIS synthetic spectra (colored lines). The residual (data minus model) spectra are shown below with 1-σ (dashed) and 3-σ (dotted) RMS values. A transition of C_2H_5CN is included in the model at ~264.292 GHz. (B) The CH_3C_3N $J = 62 \rightarrow 61$ band with modeled spectra, as in A. (C) The weighted mean best-fit vertical profiles of Titan's CH_3C_3N abundance as retrieved with NEMESIS from spectra in A and B (green, orange, and purple lines). The nominal photochemical model of Loison et al. (2015) is shown for comparison (dashed gray).

Table 2. CH_3C_3N Best Fit Model Results

Model	χ^2/n^a	Abundance^b	N (cm^{-2})^c
400 km Step	1.035	$(1.771 \pm 0.196) \times 10^{-09}$	5.727×10^{12}
500 km Step	1.020	$(1.139 \pm 0.120) \times 10^{-08}$	4.723×10^{12}
600 km Step	1.018	$(6.851 \pm 0.693) \times 10^{-08}$	4.400×10^{12}
700 km Step	1.018	$(3.230 \pm 0.312) \times 10^{-07}$	3.860×10^{12}
800 km Step	1.018	$(2.152 \pm 0.198) \times 10^{-06}$	5.607×10^{12}
Linear Gradient	1.019		4.709×10^{12}
Point 1 (400 km)		$(4.093 \pm 0.339) \times 10^{-10}$	
Point 2 (1100 km)		$(2.675 \pm 0.222) \times 10^{-06}$	
Loison et al. (2015) Scaling	0.978	0.343 ± 0.115	9.741×10^{12}

NOTE— [a] Reduced-χ^2 values, where n = number of data points minus model degrees of freedom. [b] Retrieved abundances are presented for all models except the scaling retrieval of the Loison et al. (2015) model, where the scale factor and error are shown. The abundance values for the two (high and low) pressure point fits of the linear gradient model are listed. [c] Total column density integrated up to 1200 km.

flexibility in the profile to achieve a good fit, p_2 and q_2 were set to be constrained by the INMS measurements of $C_4H_3NH^+$ ions in Titan's upper atmosphere (∼1100 km), with the inferred neutral C_4H_3N abundance ranging between (2–4)×10^{-6} (Vuitton et al., 2007; Vuitton et al., 2019). Here, CH_3C_3N lines were only sensitive to abundances above 400 km ($p_1 = 1.19 \times 10^{-2}$ mbar), resulting in $q_1 = 0.41$ ppb and $q_2 = 2.68$ ppm at 1100 km ($p_2 = 7.64 \times 10^{-8}$ mbar). The resulting synthetic spectra and gradient profile are shown in Fig. 3 (purple lines). The integrated column density of this linear gradient model is 4.71×10^{12}, in broad agreement with the step model profiles.

Finally, we attempted to fit the spectra by retrieving a multiplicative scaling factor applied to the photochemical model profile of Loison et al. (2015). This profile produced a good fit when scaled by a factor of 0.34 of the original nominal model (Fig. 3A and B, green spectra; Fig. 3C, green line). The resulting column density of 9.74×10^{12}, however, is higher than that of the best fit step or gradient models by a factor of ∼ 1.7–2.5 (Table 2).

4. DISCUSSION & CONCLUSIONS

Though we were able to fit both detected CH_3C_3N spectral bands with a variety of vertical profiles (Fig. 3C), the relatively short photochemical lifetime of CH_3C_3N – between 10^4–10^6 seconds from 400–800 km (Loison et al., 2015) – suggests that a vertically uniform mixing ratio profile may not be physically realistic. As such, the scaled profile of Loison et al. (2015) and linear gradient (Fig. 3C, green and purple

lines, respectively) are favored for the abundance profile of CH_3C_3N. These profiles depict the formation of CH_3C_3N in Titan's upper atmosphere 400–500 km (similar to its protonated counterpart, $C_4H_3NH^+$) with decreasing abundance as a function of depth as the result of photodissociation and lack of reactive radicals (such as CN and CCN). The dissociation of CH_3C_3N has yet to be studied in detail, though the pathways CH_2C_3N + H or CH_3 + C_3N have been suggested by Loison et al. 2015; alternatively, by analogy with HC_3N (see Huebner & Mukherjee, 2015; Vuitton et al., 2019), we might expect that CH_3C_3N photolysis instead yields CH_3C_2 and CN. We find insufficient CH_3C_3N abundance at altitudes < 400 km to properly identify the dependence of the mixing ratio on altitude in Titan's stratosphere and below, where GCR chemistry may play an additional role in complex molecule formation.

Our retrieved abundances above 700 km (Table 2) are in good agreement with the estimated CH_3C_3N upper limit of 2.5×10^{-7} by Cerceau et al. (1985) based on the derived stratospheric HCN and HC_3N abundances in Titan's north pole (then in winter) from *Voyager-1* infrared measurements. Further, the derived column abundances from this work between $(3.8–5.7)\times10^{12}$ are in agreement with the lower value of 5.5×10^{12} found in the laboratory simulations by Coll et al. (1999). The scaling of the nominal Loison et al. (2015) profile by a factor of 0.34 places it within 50% of their simulated profiles (see their Fig. 14), which show significant spread due to the unknown reaction rate coefficients for the production and loss of CH_3C_3N. The linear gradient low-pressure point (q_2), 800 km step, and scaled profile of the Loison et al. (2015) model results here are all in agreement with the inferred C_4H_3N abundance of 2×10^{-6} at 1100 km from the Cassini T40 flyby INMS measurements by Vuitton et al. (2019).

While the Loison et al. (2015) CH_3C_3N model corroborates the upper atmospheric abundance of C_4H_3N inferred by Vuitton et al. (2007) from the T5 INMS measurements (a factor of 2 higher than those derived from T40 in Vuitton et al., 2019), a large disparity between the photochemical models (and within the ensemble of models produced by Loison et al., 2015) arises in the lower atmosphere due to the poorly constrained C_4H_3N branching ratios and reaction rate coefficients at temperatures appropriate for Titan. Aside from electron dissociative recombination of $C_4H_3NH^+$ (Vuitton et al., 2007), neutral production of CH_3C_3N can occur in a few ways, as found through crossed beam experiments, theoretical and photochemical modeling studies (Huang et al., 1999; Balucani et al., 2000; Zhu et al., 2003; Wang et al., 2006; Loison et al., 2015). First, through the reactions of larger hydrocarbons with CN radicals:

$$CH_3CCH + CN \longrightarrow CH_3C_3N + H, \quad (1)$$

$$CH_3CCCH_3 + CN \longrightarrow CH_3C_3N + CH_3. \quad (2)$$

Similarly, with CCN radicals following their formation through H + HCCN (Osamura & Petrie, 2004; Takayanagi et al., 1998) and subsequent reactions with ethylene:

$$CCN + C_2H_4 \longrightarrow CH_3C_3N + H, \tag{3}$$

or through the chain beginning with acetylene:

$$\begin{aligned} CCN + C_2H_2 &\longrightarrow HC_4N + H, \\ HC_4N + H &\xrightarrow{M} CH_2C_3N, \\ CH_2C_3N + H &\xrightarrow{M} CH_3C_3N. \end{aligned} \tag{4}$$

While both reactions 3 and 4 are found to be equally likely by Loison et al. (2015), the production of CCN via H + HCCN is not well constrained, and the synthesis of CH_3C_3N through CN radicals (Eqs. 1,2) are not included in their photochemical model. Additionally, cyanoallene may be produced through reactions 1–4 instead of (or in addition to) methylcyanoacetylene. CH_3C_3N itself may form the protonated species, $C_4H_3NH^+$, through reactions with the $HCNH^+$ and $C_2H_5^+$ ions producing HCN and C_2H_4, respectively (Vuitton et al., 2007). The other mechanism for forming $C_4H_3NH^+$ is through the combination of HCN and l-$C_3H_3^+$, though the reaction rate coefficient for this reaction and the abundance of l-$C_3H_3^+$ are unknown (Vuitton et al., 2007). As such, the production and loss pathways for both $C_4H_3NH^+$ and CH_3C_3N require further investigation.

The detection of CH_3C_3N here supports the previous identification of $C_4H_3NH^+$ at $m/z = 66$ from Cassini/INMS observations, and adds a valuable component to Titan's extensive atmospheric photochemistry while revealing the need for further laboratory and photochemical model studies detailing the production and dissociation of Titan's larger nitriles. The retrieved column density and upper atmospheric abundances agree with previous INMS measurements, laboratory and photochemical model predictions, though the lack of sensitivity to Titan's lower atmosphere through the $J = 64 \rightarrow 63$ and $J = 62 \rightarrow 61$ rotational bands inhibits our investigation of the stratospheric abundance and condensation of CH_3C_3N. However, these results provide insights into the possible shape of the full vertical profile through the scaling of the model produced by Loison et al. (2015), and place constraints on the total column density of CH_3C_3N in Titan's atmosphere to aid in the determination of the production ratio of methylcyanoacetylene to cyanoallene, and the abundance of products resulting from the photodissociation both species. The detection of CH_3C_3N also provides the incentive for future observations of Titan at long wavelengths in the pursuit of further complex, polar nitriles (such as C_3H_7CN and HC_5N) that are predicted to exist in Titan's atmosphere. Finally, as with other trace species with fairly short photochemical lifetimes (compared to dynamical timescales), CH_3C_3N may have a complex and temporally variable spatial distribution that can be investigated with ALMA in the future through higher angular resolution observations.

5. ACKNOWLEDGMENTS

The authors would like to thank N. Chanover, M. Dobrijevic, and J.C. Loison for their previous efforts in the proposed ALMA observations targeting CH_3C_3N and other molecules in Titan's atmosphere, and to R. Cosentino for discussions regarding ALMA bandpass smoothing.

AET was supported by the NASA Astrobiology Postdoctoral Program in association with the NASA Astrobiology Institute (NAI) and the Universities Space Research Association. MAC was funded by the National Science Foundation Grant #AST-1613987. CAN and MAC received funding from NASA's Solar System Observations Program. CAN was supported by the NAI. NAT and PGJI were funded by the UK Science and Technology Facilities Council.

This paper makes use of the following ALMA data: ADS/JAO.ALMA#2019.1.00783.S. ALMA is a partnership of ESO (representing its member states), NSF (USA) and NINS (Japan), together with NRC (Canada) and NSC and ASIAA (Taiwan) and KASI (Republic of Korea), in cooperation with the Republic of Chile. The Joint ALMA Observatory is operated by ESO, AUI/NRAO and NAOJ. The National Radio Astronomy Observatory is a facility of the National Science Foundation operated under cooperative agreement by Associated Universities, Inc.

APPENDIX

A. APPLICATION OF ALMA BANDPASS SMOOTHING

Bandpass calibration is practiced in radio and (sub)millimeter observations through the use of an off-source target to remove frequency (and sometimes time) dependent fluctuations in visibility amplitudes and phases across spectral windows, which often manifest as continuum ripples or undulations in target spectra. Proper bandpass calibration can increase the dynamic range of (sub)mm images, and facilitates the measurement of weak (or broad) spectroscopic features. Often, quasi-stellar objects with well characterized properties are observed for short durations (typically 2–30 minutes) with ALMA to remove visibility artifacts as a function of frequency, which improves variations in amplitude and phase to $\lesssim 0.1\%$ and $\lesssim 0.3$ deg in ALMA Band 3–6, respectively (though edge channels are still routinely removed due to large amplitude changes).

It has been shown that noise from variations in frequency in the bandpass calibration solution can approach system noise (i.e. random noise in radio antenna receivers) for short bandpass calibrator integrations, but the application of bandpass smoothing (applied to the calibration target solution) or additional calibrator integration time can further reduce the total spectral RMS through the reduction of bandpass artifacts (Yamaki et al., 2012). This has been demonstrated to be effective for ALMA as well

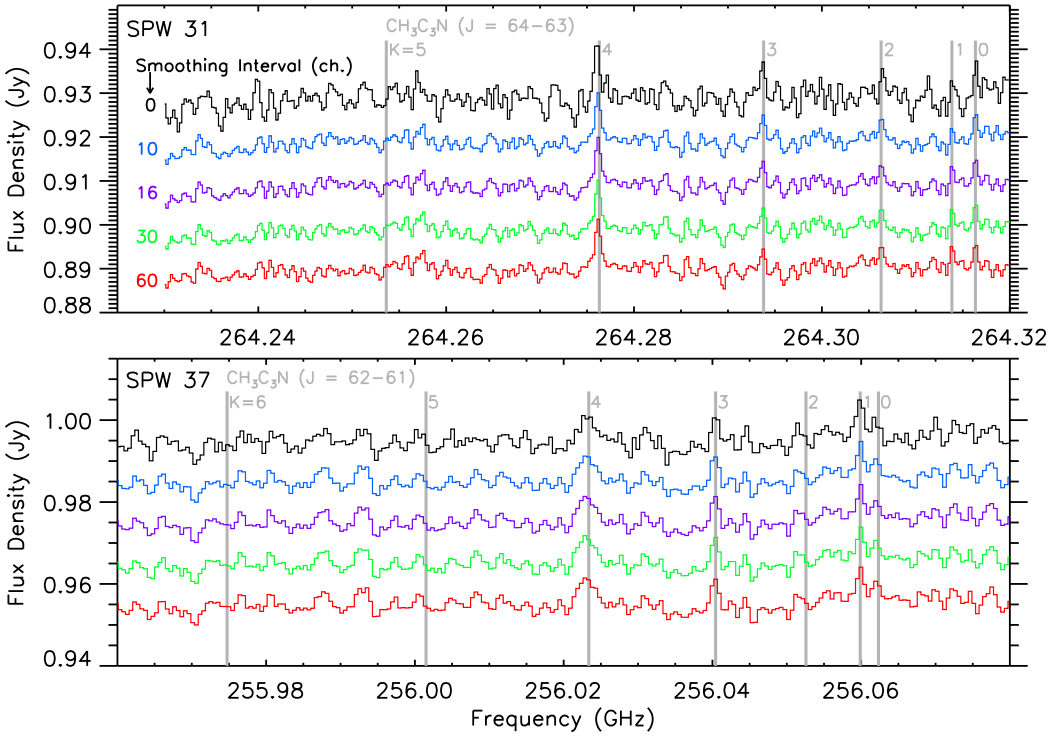

Figure 4. (Top) Disk-averaged Titan spectra from spectral window 31 showing the effects of various bandpass smoothing intervals: 0 (black, default), 10 (blue), 16 (purple) 30 (green), and 60 channels (red). Spectra are separated by 10 mJy for visibility. Transitions of the CH_3C_3N $J = 64 \rightarrow 63$ band are marked in gray. Spectral lines with significant flux (e.g. HC_3N $\nu_6 = 1$) were removed for clarity (see Fig. 1, Table 1). (Bottom) Spectra are shown as in the top panel, but for SPW 37. Smoothing was applied for the same number of channel intervals, and denoted by the same colors as the top panel. Transitions of CH_3C_3N $J = 62 \rightarrow 61$ are marked in gray.

for spectral intervals with $\Delta\nu < 100$ MHz[1]. As such, though the total integration time of SG2 was a factor ~ 2 more than that of SG3 in our observations (see Section 2), the corresponding spectral noise was not initially decreased by $\sim\sqrt{2}$ due to the limitations of noise from the default bandpass calibrator solutions. Here, we varied the bandpass solution interval to apply smoothing to the bandpass calibration function by averaging over a range of channels. Fig. 4 shows the resulting disk-averaged spectra for SPW 31 and SPW 37 after using between 0–60 channel bandpass smoothing solutions. Here, the effects of bandpass smoothing are particularly evident in the comparison between 0 and 10–30 channel solution intervals.

We found that after applying a smoothing interval of 16 channels (7.81 MHz in SG2 SPW 31, 15.6 MHz in SG3 SPW 37) the RMS decreased by a factor of 1.67 in SPW 31 and by a factor of 1.12 in SPW 37 (Fig. 5A). The resulting RMS in SPW 31 (1.33 mJy) was then a factor of $\sim\sqrt{2}$ less than in SPW 37 (1.88 mJy). Additionally, the decrease in spectral noise from the CH_3C_3N bands reduced the apparent peak line flux density

[1] See ALMA Technical Notes 15.

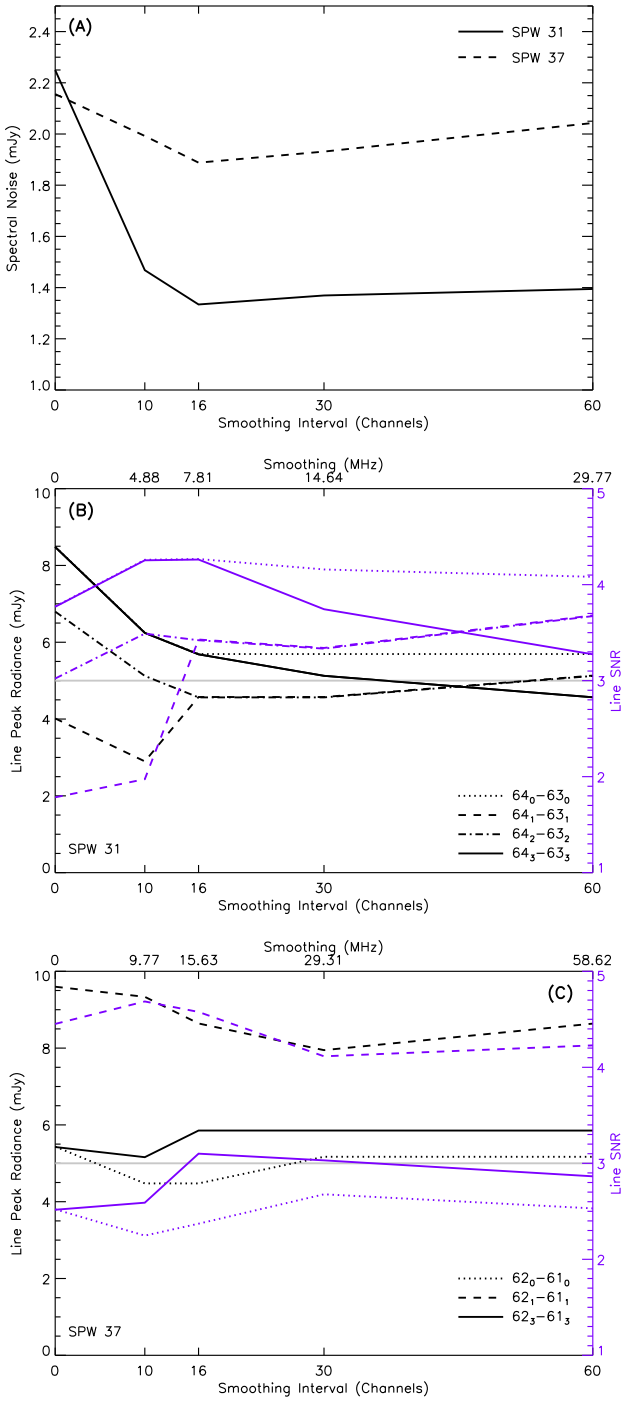

Figure 5. (A) The response of the root mean square noise in spectral window 31 (solid) and 37 (dashed) as a function of bandpass smoothing interval in channels. (B) The calculated line peak flux (line minus continuum) as a function of smoothing interval for all four detected CH_3C_3N transitions in SPW 31 (black lines) and the resulting signal-to-noise ratio (purple lines and corresponding y-axis) when divided by the RMS values in (A). The 3-σ threshold is marked in gray for reference. (C) Same as (B), but for SPW 37. The CH_3C_3N $J = 62_2 \rightarrow 61_2$ transition is not plotted here, as the line flux remained at the noise level for all bandpass smoothing intervals (Figs. 3B, 4).

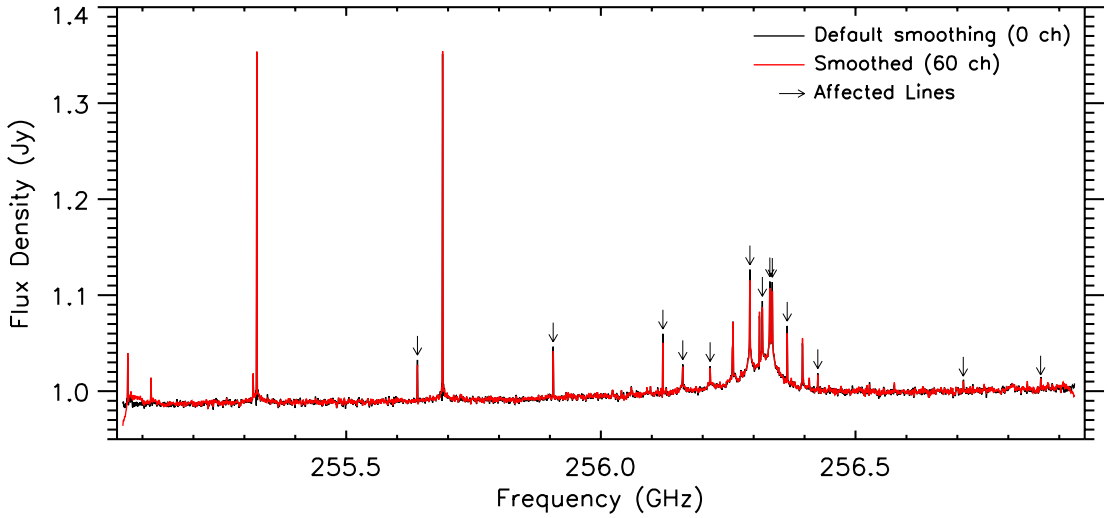

Figure 6. Comparison of disk-averaged Titan spectra from SG3 (SPW 37) with default (black) and 60 channel bandpass smoothing (red) applied. Transitions with reduced apparent line peak fluxes after the decrease of RMS noise as a result of bandpass smoothing are marked with arrows. Bandpass artifacts induced by excessive smoothing are apparent towards the bandwidth edges (red spectrum < 255.15 GHz and > 256.9 GHz).

of some transitions by $\sim$ 1-σ, but the corresponding decrease in RMS improved the overall SNR in most lines of both spectral bands (Fig. 5B,C). An example of the removal of additive noise peaks from spectral line fluxes after bandpass smoothing is shown in Fig. 6. We found that 16 channel smoothing resulted in the optimal increase in SNR across all lines of both spectral bands for CH_3C_3N. Increased smoothing ($>$ 20–30 MHz) showed diminishing returns on spectral RMS, though caution should be taken when averaging over large intervals, as the continuum may be aversely affected – particularly for channels close to either edge of the bandwidth (Fig. 6, red spectrum). The optimal channel interval depends on spectral resolution, frequency, bandpass and target integration time, so we encourage observers to experiment with multiple bandpass smoothing solutions to determine the appropriate solution interval for observations with ALMA.

The application of bandpass smoothing in radio spectra has previously been studied by Yamaki et al. (2012) with similar results in RMS improvements after increased channel smoothing intervals and additional time on bandpass calibration sources. To facilitate the detection of additional trace gases in planetary atmospheres, bandpass smoothing may be applied to ALMA data with long integration times. Here, we find limited increase in line SNR for SG3 (Fig. 5A and C), similar to previous efforts to detect c-C_3H_2 in ALMA observations of Titan (Nixon et al., 2020); however, the significant decrease in RMS in SG2 (Fig. 5A and B) promotes the use of bandpass smoothing for Titan observations with total (on source) integration times of $\gtrsim$ 2 hours. Additionally, increased integration time on bandpass calibrators, which is available under specific well-justified conditions by ALMA, may further decrease the spectral RMS (Yamaki et al., 2012).

REFERENCES

Anttila, R., Horneman, V., Koivusaari, M., & Paso, R. 1993, Journal of Molecular Spectroscopy, 157, 198, doi: 10.1006/jmsp.1993.1016

Balucani, N., Asvany, O., Osamura, Y., et al. 2000, Planetary and Space Science, 48, 447 , doi: 10.1016/S0032-0633(00)00018-0

Belloche, A., Müller, H. S. P., Menten, K. M., Schilke, P., & Comito, C. 2013, A&A, 559, A47, doi: 10.1051/0004-6361/201321096

Bester, M., Tanimoto, M., Vowinkel, B., Winnewisser, G., & Yamada, K. 1985, Z. Naturforsch. Sect. A – J. Phys. Sci., 38, 64, doi: 10.1515/zna-1983-0112

Bester, M., Yamada, K., Winnewisser, G., et al. 1984, A&A, 137, L20

Broten, N. W., MacLeod, J. M., Avery, L. W., et al. 1984, ApJL, 276, L25, doi: 10.1086/184181

Cerceau, F., Raulin, F., Courtin, R., & Gautier, D. 1985, Icarus, 62, 207, doi: 10.1016/0019-1035(85)90118-6

Coll, P., Coscia, D., Smith, N., et al. 1999, P&SS, 47, 1331, doi: 10.1016/S0032-0633(99)00054-9

Cordiner, M. A., Nixon, C. A., Charnley, S. B., et al. 2018, ApJ, 859, L15, doi: 10.3847/2041-8213/aac38d

Cordiner, M. A., Teanby, N. A., Nixon, C. A., et al. 2019, AJ, 158, 76, doi: 10.3847/1538-3881/ab2d20

Cordiner, M. A., Nixon, C. A., Teanby, N. A., et al. 2014, ApJ, 795, L30, doi: 10.1088/2041-8205/795/2/L30

Cordiner, M. A., Palmer, M. Y., Nixon, C. A., et al. 2015, ApJ, 800, L14, doi: 10.1088/2041-8205/800/1/L14

Endres, C. P., Schlemmer, S., Schilke, P., Stutzki, J., & Müller, H. S. P. 2016, Journal of Molecular Spectroscopy, 327, 95, doi: 10.1016/j.jms.2016.03.005

Fulchignoni, M., Ferri, F., Angrilli, F., et al. 2005, Nature, 438, 785, doi: 10.1038/nature04314

Hörst, S. M., Yelle, R. V., Buch, A., et al. 2012, Astrobiology, 12, 809, doi: 10.1089/ast.2011.0623

Huang, L. C. L., Balucani, N., Lee, Y. T., Kaiser, R. I., & Osamura, Y. 1999, JCP, 111, 2857, doi: 10.1063/1.479567

Huebner, W., & Mukherjee, J. 2015, P&SS, 106, 11 , doi: 10.1016/j.pss.2014.11.022

Iino, T., Sagawa, H., & Tsukagoshi, T. 2020, ApJ, 890, 95, doi: 10.3847/1538-4357/ab66b0

Irwin, P. G. J., Teanby, N. A., de Kok, R., et al. 2008, J. Quant. Spec. Radiat. Transf., 109, 1136, doi: 10.1016/j.jqsrt.2007.11.006

Kisiel, Z., Nixon, C. A., Cordiner, M. A., Thelen, A. E., & Charnley, S. B. 2020, Journal of Molecular Spectroscopy, 372, 111324, doi: 10.1016/j.jms.2020.111324

Lai, J. C.-Y., Cordiner, M. A., Nixon, C. A., et al. 2017, AJ, 154, 206, doi: 10.3847/1538-3881/aa8eef

Lellouch, E., Gurwell, M. A., Moreno, R., et al. 2019, Nature Astronomy, 3, 614, doi: 10.1038/s41550-019-0749-4

Loison, J. C., Hébrard, E., Dobrijevic, M., et al. 2015, Icarus, 247, 218, doi: 10.1016/j.icarus.2014.09.039

Lovas, F. J., Remijan, A. J., Hollis, J. M., Jewell, P. R., & Snyder, L. E. 2006, ApJL, 637, L37, doi: 10.1086/500431

Moïses, A., Boucher, D., Burie, J., Demaison, J., & Dubrulle, A. 1982, Journal of Molecular Spectroscopy, 497, doi: 10.1016/0022-2852(82)90118-7

Molina-Cuberos, G. J., Schwingenschuh, K., López-Moreno, J. J., et al. 2002, JGR (Planets), 107, 5099, doi: 10.1029/2000JE001480

Molter, E. M., Nixon, C. A., Cordiner, M. A., et al. 2016, AJ, 152, 1, doi: 10.3847/0004-6256/152/2/42

Müller, H. S. P., Schlöder, F., Stutzki, J., & Winnewisser, G. 2005, Journal of Molecular Structure, 742, 215, doi: 10.1016/j.molstruc.2005.01.027

Müller, H. S. P., Thorwirth, S., Roth, D. A., & Winnewisser, G. 2001, A&A, 370, L49, doi: 10.1051/0004-6361:20010367

Nixon, C. A., Achterberg, R. K., Teanby, N. A., et al. 2010, Faraday Discuss., 147, 65, doi: 10.1039/c003771k

Nixon, C. A., Thelen, A. E., Cordiner, M. A., et al. 2020, AJ (in press)

Osamura, Y., & Petrie, S. 2004, J. of Phys. Chemistry A, 108, 3615, doi: 10.1021/jp037817+

Palmer, M. Y., Cordiner, M. A., Nixon, C. A., et al. 2017, Sci. Adv., 3, doi: 10.1126/sciadv.1700022

Schinder, P. J., Flasar, F. M., Marouf, E. A., et al. 2012, Icarus, 221, 1020, doi: 10.1016/j.icarus.2012.10.021

Serigano, J., Nixon, C. A., Cordiner, M. A., et al. 2016, ApJ, 821, L8, doi: 10.3847/2041-8205/821/1/L8

Takayanagi, T., Kurosaki, Y., Misawa, K., et al. 1998, J. of Phys. Chemistry A, 102, 6251, doi: 10.1021/jp9811631

Teanby, N. A., Irwin, P. G. J., de Kok, R., & Nixon, C. A. 2010, ApJ, 724, L84, doi: 10.1088/2041-8205/724/1/L84

Teanby, N. A., Irwin, P. G. J., Nixon, C. A., et al. 2013, Planet. Space Sci., 75, 136, doi: 10.1016/j.pss.2012.11.008

Teanby, N. A., Cordiner, M. A., Nixon, C. A., et al. 2018, AJ, 155, 251, doi: 10.3847/1538-3881/aac172

Thelen, A. E., Nixon, C. A.and Cordiner, M. A., Charnley, S. B., Irwin, P. G. J., & Kisiel, Z. 2019a, AJ, 157, 219, doi: 10.3847/1538-3881/ab19bb

Thelen, A. E., Nixon, C. A., Chanover, N. J., et al. 2018, Icarus, 307, 380, doi: 10.1016/j.icarus.2017.10.042

—. 2019b, Icarus, 319, 417, doi: 10.1016/j.icarus.2018.09.023

Thompson, W. R., Henry, T. J., Schwartz, J. M., Khare, B. N., & Sagan, C. 1991, Icarus, 90, 57, doi: 10.1016/0019-1035(91)90068-5

Vuitton, V., Yelle, R. V., Klippenstein, S. J., Hörst, S. M., & Lavvas, P. 2019, Icarus, 324, 120, doi: 10.1016/j.icarus.2018.06.013

Vuitton, V., Yelle, R. V., & McEwan, M. J. 2007, Icarus, 191, 722, doi: 10.1016/j.icarus.2007.06.023

Wang, J., Ding, Y.-h., & Sun, C.-c. 2006, ChemPhysChem, 7, 710, doi: 10.1002/cphc.200500548

Yamaki, H., Kameno, S., Beppu, H., Mizuno, I., & Imai, H. 2012, PASJ, 64, 118, doi: 10.1093/pasj/64.5.118

Zhu, Z., Zhang, Z., Huang, C., et al. 2003, J. of Phys. Chemistry A, 107, 10288, doi: 10.1021/jp030763j